Article

Structure

Capsid Structure of a Freshwater Cyanophage Siphoviridae Mic1

Graphical Abstract

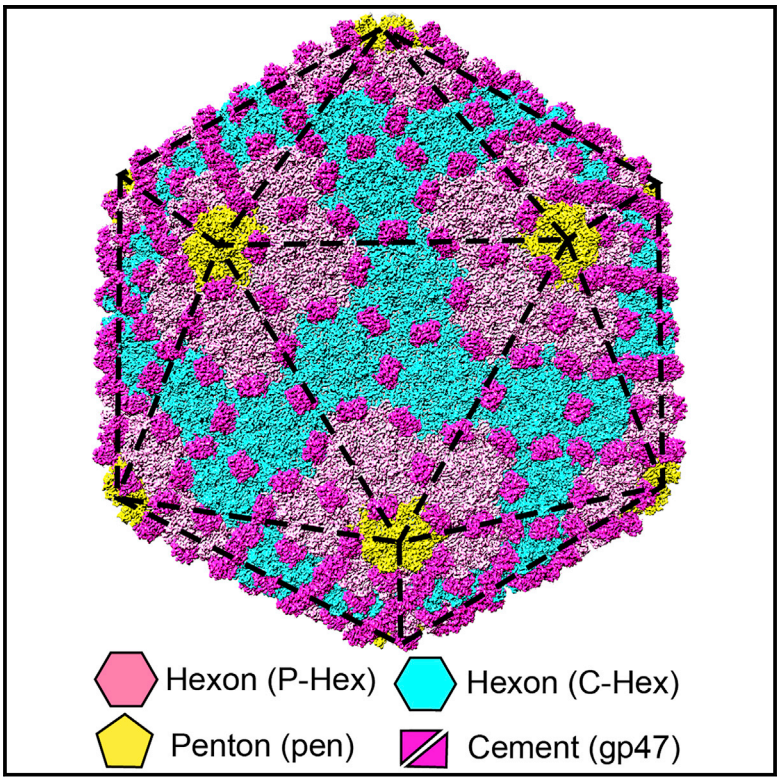

Highlights

- A new freshwater long-tailed cyanophage Mic1 was identified from Lake Chaohu
- The capsid structure of Mic1 at 3.5-Å resolution was solved by cryo-EM
- Mic1 capsid adopts a mortise-and-tenon assembly mechanism

Authors

Hua Jin, Yong-Liang Jiang, Feng Yang, ..., Jue Ju, Yuxing Chen, Cong-Zhao Zhou

Correspondence

cyxing@ustc.edu.cn (Y.C.), zcz@ustc.edu.cn (C.-Z.Z.)

In Brief

The cryo-EM structure of a freshwater cyanophage Mic1 capsid reveals the structural variations of the major capsid protein and a novel fold of the cement protein, which enable the assembly of the icosahedral capsid via a mortise-and-tenon pattern.

Jin et al., 2019, Structure 27, 1–9
October 1, 2019
https://doi.org/10.1016/j.str.2019.07.003

CellPress

Please cite this article in press as: Jin et al., Capsid Structure of a Freshwater Cyanophage Siphoviridae Mic1, Structure (2019), https://doi.org/10.1016/j.str.2019.07.003

Structure
Article

CellPress

Capsid Structure of a Freshwater Cyanophage Siphoviridae Mic1

Hua Jin,[1,2] Yong-Liang Jiang,[1,2] Feng Yang,[1] Jun-Tao Zhang,[1] Wei-Fang Li,[1] Ke Zhou,[1] Jue Ju,[1] Yuxing Chen,[1,*] and Cong-Zhao Zhou[1,3,*]

[1]Hefei National Laboratory for Physical Sciences at the Microscale and School of Life Sciences, University of Science and Technology of China, Hefei, Anhui 230026, China

[2]These authors contributed equally

[3]Lead Contact

*Correspondence: cyxing@ustc.edu.cn (Y.C.), zcz@ustc.edu.cn (C.-Z.Z.)

https://doi.org/10.1016/j.str.2019.07.003

SUMMARY

Cyanobacteria are the most abundant photosynthetic microorganisms, the global distribution of which is mainly regulated by the corresponding cyanophages. A systematic screening of water samples in the Lake Chaohu enabled us to isolate a freshwater siphocyanophage that infects *Microcystis wesenbergii*, thus termed Mic1. Using cryoelectron microscopy, we solved the 3.5-Å structure of Mic1 capsid. The major capsid protein gp40 of an HK97-like fold forms two types of capsomers, hexons and pentons. The capsomers interact with each other via the interweaved N-terminal arms of gp40 in addition to a tail-in-mouth joint along the three-fold symmetric axis, resulting in the assembly of capsid in a mortise-and-tenon pattern. The novel-fold cement protein gp47 sticks at the two-fold symmetric axis and further fixes the capsid. These findings provide structural insights into the assembly of cyanophages, and set up a platform to explore the mechanism of specific interactions and co-evolution with cyanobacteria.

INTRODUCTION

The ancient and robust cyanobacteria, also called blue-green algae, can perform photosynthesis, contributing to the majority of carbon fixation on the Earth (Rasmussen et al., 2008). However, due to the eutrophication of freshwater lakes, the hypertrophic growth of cyanobacteria in these eutrophic water bodies triggers algal bloom, which has become a severe environmental and economic problem, especially in the developing countries (Huisman et al., 2018). The common bloom-forming genera include *Aphanizomenon*, *Microcystis*, *Cylindrospermopsis*, *Dolichospermum*, *Nodularia*, *Planktothrix*, and *Trichodesmium* (Huisman et al., 2018). In recent years, Taihu, Dianchi, and other lakes in southern China have usually been full of massive algal blooms every summer (Liu and Qiu, 2007). The cyanobacterial strain *Microcystis* spp. has been the dominant species of bloom expansion (Chen et al., 2003). As the fifth largest freshwater lake in China, Lake Chaohu also suffers from seasonal algal blooms.

The growth and fluctuation of the dominant species of cyanobacteria are mainly controlled by corresponding cyanophages (Zhang and Gui, 2018), in addition to nutrients and grazers (Paerl, 2017). The cyanophages identified to date are double-stranded DNA (dsDNA) phages that specifically infect a narrow spectrum of cyanobacterial species (Xiao et al., 2018). As we know, phages not only play roles in the processes of cell lysis, biochemical cycles, and horizontal gene transfer, but also control the community structure and function of bacteria (Weinbauer, 2004). In addition, cyanophages contribute to the nutrient recycling and regulation of microbial ecosystems, and thus might be used as environmentally friendly biological agents to the control cyanobacterial community that determines the seasonal succession of the host (Muhling et al., 2005; Thompson et al., 2011; Zeng and Chisholm, 2012). Cyanophages are widespread, with their cyanobacterial hosts in both freshwater and marine environments (Shane, 1971). During the past decades, the majority of the cyanophage research has been focused on the marine systems (Suttle, 2005), leading to the identification of a large number of marine cyanophages, which mainly infect the cyanobacteria *Prochlorococcus* (Sullivan et al., 2003) and *Synechococcus* (Suttle and Chan, 1994). By contrast, little information is available for the freshwater cyanophages, despite the first freshwater podocyanophage LPP-1, which infects filamentous cyanobacteria, being reported in 1963 (Safferman and Morris, 1963). Therefore, more investigations are needed for better understanding of the freshwater cyanophages and their potential applications in algal bloom control.

Thanks to the revolutionary development of cryoelectron microscopy (cryo-EM), the capsid structures of several bacteriophages have been determined in the past few years, owing to their large mass and high symmetry (Chen et al., 2017; Dearborn et al., 2017; Guo et al., 2014; Hryc et al., 2017; Novacek et al., 2016; Wang et al., 2018; Wikoff et al., 2000; Zhang et al., 2013; Zhao et al., 2017). These structures provided thoughtful insights into the assembly and maturation of bacteriophages. In general, the capsid shell is assembled by the pentameric and hexameric capsomers of the major capsid protein that harbors the canonical HK97-like fold (Wikoff et al., 2000). In some bacteriophages, the minor capsid proteins (also termed cement proteins) of distinct structures are positioned at the outer surface to further reinforce the shell stability (Chen et al., 2017; Wang et al., 2018; Zhang et al., 2013; Zhou and Chiou, 2015). Moreover, some bacteriophages contain the specific decorating proteins that recognize the host receptors,

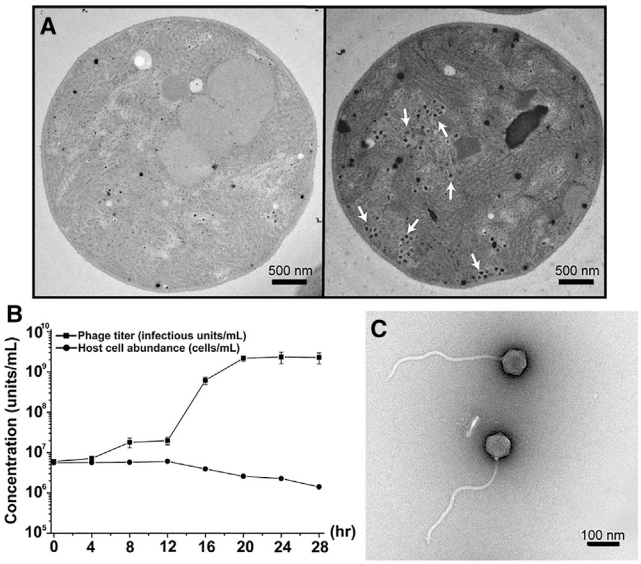

Figure 1. Infection and Characterization of Mic1

(A) Ultrathin sections of uninfected (left panel) and Mic1-infected (right panel) *M. wesenbergii* cell. The phage particles are indicated by white arrows.

(B) The one-step growth curve of Mic1 infecting the host cell *M. wesenbergii* FACHB1339. Data are presented as mean ± standard deviation from three independent experiments.

(C) Negative-staining EM image of the purified Mic1 particles.

See also Figure S1 and Table S1.

such as the highly immunogenic outer capsid protein Hoc in T4 phage (Fokine et al., 2011).

To date, only two structures of marine cyanophages, P-SSP7 and Syn5, which infect *Prochlorococcus* and *Synechococcus*, have been reported, at 4.6- and 4.7-Å resolution, respectively (Gipson et al., 2015; Liu et al., 2010). However, only the Cα backbones could be traced in the two structures, neither of which showed details of capsid assembly pattern. The limited structural information of cyanophages largely impedes our understanding of their assembly and molecular function. Here, we isolated a new cyanophage that infects *Microcystis wesenbergii*, termed Mic1, from Lake Chaohu in China. It has an isometric capsid of ~90 nm in diameter and a flexible tail of ~400 nm in length, and thus belongs to the Siphoviridae family from the viewpoint of morphology (Ackermann, 2007). Moreover, we solved the 3.5-Å cryo-EM structure of Mic1 capsid, which revealed distinct features for the capsid assembly, which is reinforced by numerous mortise-and-tenon inter-capsomer joints. These findings provided insights into the capsid assembly and a platform for further investigations of freshwater cyanophages.

RESULTS

Isolation and Characterization of Mic1

We initiated a project to systematically investigate the distribution, morphology, and abundance of cyanophages in Lake Chaohu. We collected water samples, normally 3 L for each, at different spots in the whole lake. The concentrated water samples were applied to screening of cyanophages against the 12 cyanobacterial strains, which were bought from the Freshwater Algae Culture Collection at the Institute of Hydrobiology, Chinese Academy of Sciences (Table S1). After extensive trials of extinction dilution experiments, eventually we found that *M. wesenbergii* strain FACHB1318 and FACHB1339 could be infected by the water sample collected at the entrance of the Baishitian River to the lake (location: 31°31′47.5″N, 117°23′55.3″E). After infection and plating, several round plaques were found on the agar lawn of *M. wesenbergii* cells 5 days later. Thereafter, a single plaque was chosen and inoculated to cyanobacteria grown in the liquid medium.

After cultivation for 20 h the medium became clear, indicating that the isolated cyanophage could be amplified in the host and released to medium in the mature form. The ultrathin sections of *M. wesenbergii* cells subject to cyanophage infection clearly showed hundreds of phage particles (Figure 1A), which further confirmed the amplification and assembly of cyanophages in *M. wesenbergii*; thus, we termed it Mic1. To further elucidate the physiological characteristics of this cyanophage, we measured the growth curves using one-step growth experiments. This indicated that Mic1 has a latent period of ~12 h, proliferates rapidly in the following 4 h, and finally reaches ~450 copies in each host cell of *M. wesenbergii* FACHB1339 (Figure 1B). By contrast, only ~170 Mic1 particles were released from each cell of *M. wesenbergii* FACHB1318 (Figure S1), indicating that the strain FACHB1339 has a higher efficiency in amplifying Mic1. Thus, the cyanobacterial host cells of *M. wesenbergii* FACHB1339 were applied for the amplification of cyanophage Mic1.

After amplification in liquid medium followed by separation with density gradient centrifugation, we purified the mature cyanophages of Mic1 released in the medium. Transmission electron microscopy revealed that Mic1 has an isometric head with a diameter of ~90 nm and a flexible tail of ~400 nm in length (Figure 1C), which belongs to the Siphoviridae family of phages (Ackermann, 2007). It has a cyclic genome of 92.6 kb of dsDNA that harbors 98 putative open reading frames, including the genes encoding the hypothetical capsid protein gp40 and the cement protein gp47, as well as other structural and scaffold proteins (GenBank: MN013189). The electrophoresis and mass spectrometric analysis also revealed that gp40 and gp47 are among the most abundant structural components of Mic1 (Figure S2 and Table S2).

Structure Determination and Overall Structure

To elucidate the mechanism of capsid assembly, we imaged the samples of the purified cyanophage Mic1 by cryo-EM (Figure 2A). The icosahedral reconstruction of the capsid from 9,702 virion particles gave an overall resolution of 3.5 Å for each asymmetric unit (Figures 2B and S3). The capsid adopts an icosahedral structure with a diameter of ~880 Å (Figure 2C). The high-quality cryo-EM map enabled us to manually build the model of the major capsid protein gp40 from residues Ala2 to Val347 (out of 348 residues) for the hexameric capsomer (termed hexon), and residues Ala2–Thr229 and Phe242–Val347 for the pentameric capsomer (termed penton), which are regularly positioned on the facets and vertices of the capsid, respectively (Figure 2D). Moreover, based on best matching of the map using the Mic1 genomic sequence and an all-alanine model, we assigned the minor capsid protein (also termed cement protein) to gp47 and eventually modeled the gp47 structure from residues Pro2 to

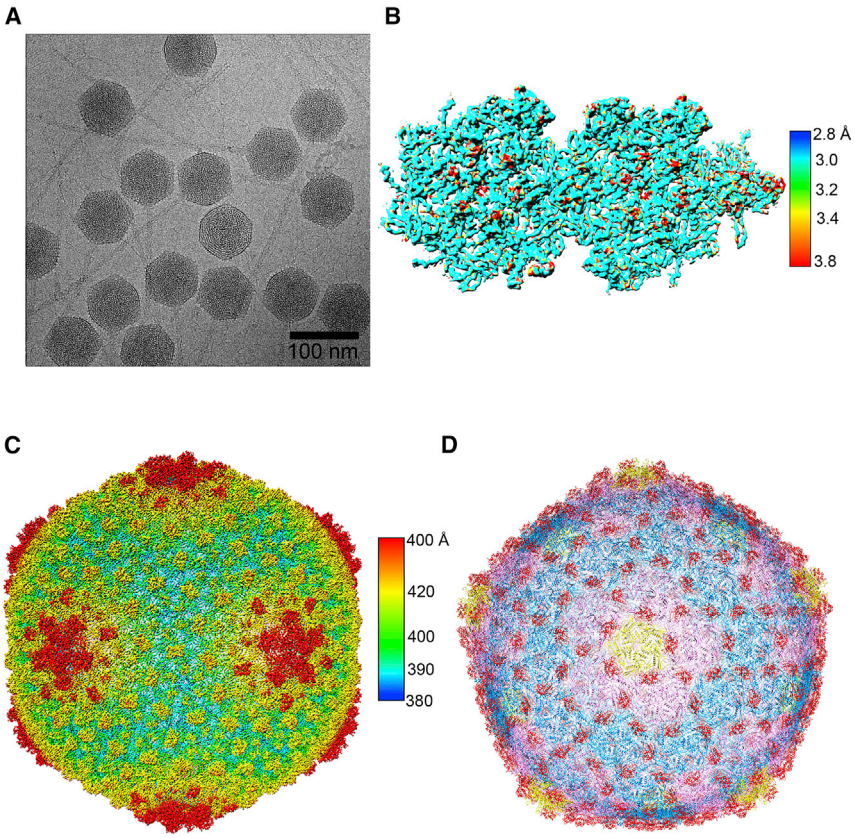

Figure 2. Cryo-EM Structure of Mic1 Capsid

(A) Representative cryo-EM image of Mic1.

(B) Local resolution map of an asymmetric unit calculated using ResMap.

(C) Cryo-EM density map of Mic1 capsid, colored radially from outside to inside in blue to red.

(D) Cartoon presentation of Mic1 capsid with differentially colored structural components (P-Hex in pink, C-Hex in cyan, penton in yellow, and cement in red).

See also Figures S2 and S3; Table S2.

Thr98 (99 residues in total) that matches the discrete patches on the outer surface of the capsid (Figure 2D). The model shows good stereochemistry and has an average real-space correlation coefficient of 0.86 (Table 1).

The isometric capsid shell of Mic1 consists of 120 hexons, 12 pentons, and 390 dimers of cement protein, or in sum 780 copies of gp40 and gp47 subunits, respectively (Figures 2C and 2D). The capsid exhibits a triangulation number T of 13 with an asymmetric unit composed of 12 hexameric gp40 subunits of two hexons, one pentameric gp40 subunit, and 13 subunits of gp47 (Figure 3A). Each gp40 subunit consists of an elongated N-terminal arm (N arm, residues 1–33), an extended loop (E loop, residues 38–78), and a peripheral domain (P domain, residues 34–37, 79–161, and 289–334), in addition to an axial domain (A domain, residues 162–169, 185–258, 279–288, and 334–348) at the center of the capsomers (Figure 3B). The overall structure of gp40 resembles the canonical HK97 fold in tailed dsDNA bacteriophages and herpes viruses (Baker et al., 2005; Wikoff et al., 2000; Zhou et al., 2014). Notably, gp40 also contains an insertion segment harboring a short helix and a bend-back loop (residues 170–184 and 259–278), which protrudes outward from the surface of capsid (Figure 3B). Sequence and structural comparisons suggested that this insertion segment in Mic1 is unique and structurally distinct from the corresponding insertions of HK97-like proteins (Figure S4) that constitute the capsids of phages (Chen et al., 2017; Zhao et al., 2017).

Notably, an asymmetric unit contains 12 hexameric gp40 subunits, all of which are structurally distinct from each other (Figure 4A). Significant structural variations occur in the N arms, E loops, and the tips of P and A domains, most likely due to the clustering of small side-chain residues. The extended N arms undergo large-scale swinging by as much as 15°, resulting in a largest positional displacement of 9 Å for the N-terminal residue Ala2 (Figure 4A). The E loops and P and A domains also bend drastically, leading to a significant movement at the distal ends of these structural elements, namely helix α1 and the P loop (residues 309–324) by ~4 Å, and the tips of the E loop and A-domain loop by ~10 Å and ~8 Å, respectively. Moreover, all of these structural elements are involved in the inter-subunit interactions. Thus, we proposed that the plasticity of these structural elements enables the oligomerization of gp40 into both hexon and penton, which further assemble into the capsid.

The Major Capsid Protein gp40 Assembles into Hexons and Pentons

Each asymmetric unit contains two types of hexon (Figure 3A), termed the peripentonal hexon (P-Hex) and the central hexon (C-Hex). Compared with P-Hex, C-Hex is relatively flat, which fulfills the curvature mostly generated by the penton vertex. The hexon has a curled shape, resulting in the assembly of a uniformly curved smooth inner surface of the capsid. Each hexon is assembled via contacts of A domains at the center, in addition to the "head-to-tail" interactions between adjacent E loops and P domains at the periphery (Figure 3C), resulting in a total buried interface area of ~2,800 Å^2 between the two adjacent subunits. Six A domains constitute the core of the hexon, centered with a twisted β barrel composed of six β9 strands. In particular, the helix α3 of one subunit packs against α4 of the adjacent subunit to form the second ring around the β barrel. The E loop from one subunit makes extensive interactions with the P domain and N arm of the neighboring subunit, which further stabilizes the hexon at the periphery (Figure 3C).

Five gp40 subunits form the penton in an interaction pattern generally similar to that in the hexon (Figure 3D). Five copies of A domain juxtapose to form the core, surrounded by the E loops and P domains, which are bent more than those in the hexon. Superposition of gp40 subunit of the penton onto that of the hexon

Table 1. Cryo-EM Data Collection, Refinement, and Validation Statistics

	Mic1 (EMDB-9774) (PDB: 6J3Q)
Data Collection and Processing	
Magnification	59,000
Voltage (kV)	300
Electron exposure (e–/Å^2)	25
Defocus range (μm)	−1 to −2
Pixel size (Å)	1.36
Symmetry imposed	I3
Initial particle images (n)	18,874
Final particle images (n)	9,702
Map resolution (Å)	3.53
FSC threshold	0.143
Map resolution range (Å)	2.72–999
Refinement	
Real-space correlation coefficient	0.86
Initial model used (PDB code)	*ab initio* model
Model resolution (Å)	3.53
FSC threshold	0.143
Map-sharpening *B* factor (Å^2)	−125.62
Model composition	
Non-hydrogen atoms	2,608,860
Protein residues	344,880
Ligands	0
B factors (Å^2)	55.35
RMSDs	
Bond lengths (Å)	0.007
Bond angles (°)	1.249
Validation	
MolProbity score	2.00
Clashscore	4.96
Poor rotamers	1.02
Ramachandran plot	
Favored (%)	80.27
Allowed (%)	19.62
Disallowed (%)	0.11

resulted an overall root-mean-square deviation (RMSD) of 0.7 Å over 249 Cα atoms (Figure 4B). Compared with the hexon, the penton undergoes significant structural variations that are required for introducing more curvature at the 12 vertices of the shell, which are essential for icosahedral capsid assembly. The relative orientation between adjacent molecules in the penton changes drastically by ~43° compared with that in the hexon. This change is mainly mediated by A domains (Figure 4C), in addition to the details of inter-subunit interactions significantly different between pentons and hexons. Residues Val218 to Ala245 in the penton adopt a drastically different conformation from that in the hexon. Within this region, the C-terminal moiety (residues Val218–Ala221) of helix α4 in the hexon disrupts and refolds into a loop in the penton (Figure 4C). Accompanying this helix-to-loop transition, the side chain of residue Phe219 shifts by as much as ~11 Å. In the hexon, Phe219 stacks against Phe230 of the adjacent subunit and Phe242, whereas in the penton, Phe219 flips to the opposite direction and inserts into a hydrophobic pocket formed by helices α3, α4, and the adjacent loops via hydrophobic interactions with residues Met188, Tyr215, and Val218 (Figure 4C). Consequently, the A domain in the penton rolls along its adjacent counterpart, leading to a significant bending between two neighboring molecules, thereby generating the curvature. Moreover, the segments (residues Arg223–Ile227) at the central pore show drastic structural rearrangements, from a β barrel in the hexon to a pore composed of five loops in the penton (Figures 3C, 3D, and 4C). As a result, the central pore of the hexon has a diameter of 3.6 Å, which is much smaller than that of 6.8 Å in the penton (Figures 3C and 3D). Notably, this β-to-loop transition of the central pore has not been observed in other bacteriophages. Furthermore, owing to the β-to-loop transition, the side chain of Arg223 points outward from the central pore in the hexon, whereas it points toward the innermost of the central pore in the penton (Figure 4C). The inner surfaces of the penton and hexon show a discrete distribution of electrostatic potential (Figures S5A and S5B). By contrast, the T4 phage harbors a generally acidic inner surface of the capsid, which implies that the genomic dsDNA will not stick to the inner surface of T4, making it easier for the ejection of dsDNA out of the capsid upon infecting the host cell (Chen et al., 2017). However, due to the lack of high-resolution structures of the capsid-DNA complex, the fine packaging mechanism of the genome within a phage capsid remains unknown.

The Cement Protein gp47 Adopts a Novel Structure

In total, 390 copies of the gp47 dimer stick on the surface outside of the icosahedral capsid (Figure 2D). Each gp47 molecule has 99 residues, and folds into an N-terminal two-stranded antiparallel β sheet followed by three α helices (Figure 5A). Two subunits run across each other to form a highly interweaved dimer, which is composed of a four-stranded β sheet packing against six α helices (Figure 5B). The entangled gp47 dimer has a total interface area of ~2,600 Å^2, which is mainly mediated by hydrophobic interactions via three α helices, in addition to several hydrogen bonds formed by β2 from each subunit. A structural similarity search against gp47 using the DALI server (Holm and Sander, 1993) produced a few hits (Table S3). The top hit is 50S ribosomal protein L6P with a *Z* score of 2.7 (Lecompte et al., 2002). Superposition of gp47 onto L6P reveals an RMSD of 6.1 Å over 67 Cα atoms. Further structural classification against the SCOP database (http://scop.mrc-lmb.cam.ac.uk/scop/) found no protein that harbors a similar fold. All of these results suggested that gp47 represents a novel fold in the α+β class.

At the two-fold axis of the icosahedral capsid, each interweaved gp47 dimer is positioned upon the interface of each pair of adjacent capsomers (Figure 3A). It is worth noting that some bacteriophages of known structure also possess the cement protein (Baker et al., 2013; Chen et al., 2017; Novacek et al., 2016; Zhang et al., 2013). For example, the cement proteins gp10 of epsilon15 phage (Baker et al., 2013) and Bbp16 of BPP-1 phage (Zhang et al., 2013) adopt a similar dimeric structure of a jellyroll fold that contains two β sheets. In addition, both gp10 and Bbp16 are positioned at the two-fold axis to stabilize the adjacent capsomers by salt bridges. By contrast, the cement protein Soc of T4 phage contains a three-stranded

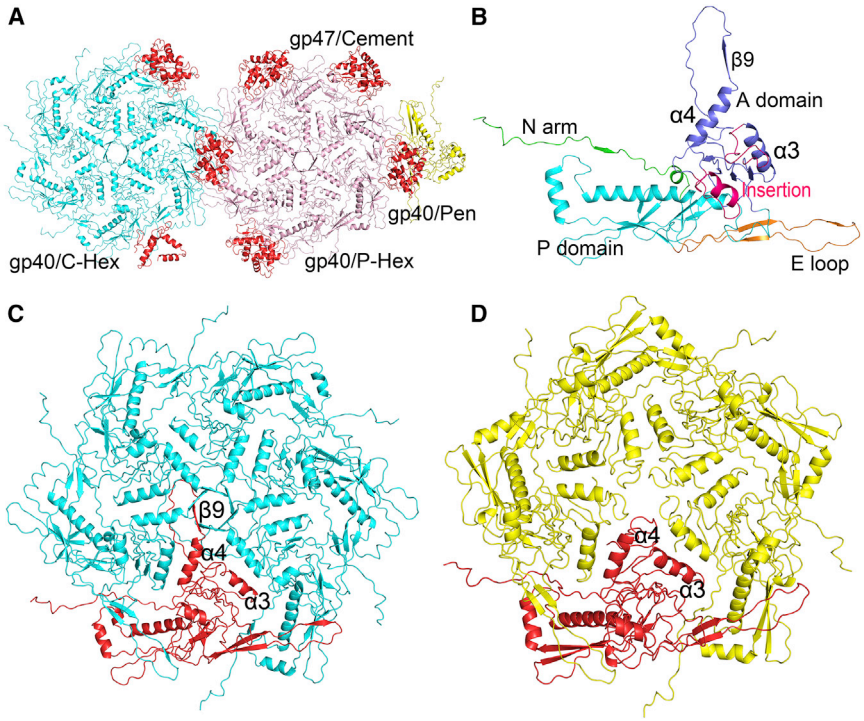

Figure 3. Structure of the Hexon and Penton

(A) Cartoon presentation of an asymmetric unit of the Mic1 capsid. The P-Hex and C-Hex are shown in pink and cyan, respectively, whereas the cement proteins are shown in red.

(B) Overall structure of the major capsid protein gp40, with the domains differentially colored.

(C) Structure of the hexon with five subunits colored in cyan and one in red.

(D) Structure of the penton with four subunits colored in yellow and one in red.

See also Figures S4, S5, and S8.

β sheet packing against two α helices (Qin et al., 2010). Three Soc subunits form a trimer around quasi-three-fold axes and interact with the I-domain linkers and the N terminus of the hexon by hydrogen bonds (Chen et al., 2017). In the case of Tw1 phage, the trimeric cement protein gp56 has two domains of a similar fold that consists of four β strands and connecting loops (Wang et al., 2018). The gp56 trimer at the three-fold axis interacts with the major capsid proteins and acts as a triple clamp to join together three neighboring capsomers. Compared with the cement proteins of other bacteriophages (Figure S6), gp47 of Mic1 shows not only a novel fold, but also a distinct interaction pattern with the capsomers. These findings also suggest a divergent evolution event that confers the cement proteins of distinct structures and interaction patterns to help the assembly of major capsid proteins that have a similar fold.

Interaction Pattern between the Capsomers

Adjacent capsomers are interlocked by mutually penetrating structural elements from the E loops, P domains, and N arms (Figure 6A), in an overall interaction mode resembling that of phages HK97 and Sf6 (Wikoff et al., 2000; Zhao et al., 2017), but exhibiting significant differences at the interfaces. Around the three-fold axis, three capsomers interact with each other via a double-layered interface (Figure 6A). The outer layer is formed by three E loops, whereas the inner layer is formed by three P loops from the surrounding capsomers. In detail, the P domain and the E loop from the adjacent subunit in the same capsomer form a lock, which is able to perfectly accommodate a key composed of helix α1 and P loop of P domain from another capsomer, in a cyclic tail-in-mouth manner (Figure 6A, right panel). At the interface along the two-fold axis, the inter-capsomer interactions are further reinforced by N arms. The N arm, which is a highly extended ~60 Å in length, sticks against the adjacent capsomer via main-chain interactions with the neighboring N arm (Figure 6B). All of these structural elements exhibit sequential structural complementarity at the interfaces, reminiscent of a mortise-and-tenon joint.

At the interface of each pair of adjacent capsomers, the dimeric gp47 forms a tenon-like structure to interlock the neighboring capsomers (Figure 6C). Each gp47 dimer interacts with four gp40 subunits that belong to two adjacent capsomers (Figure 3A), resulting in a total interface area of ~2,400 Å^2. Notably, the four-stranded β sheet of the gp47 dimer adheres to the two antiparallel N arms, thus contributing to the majority of interactions (Figure 6C). The interface is mainly mediated by van der Waals interactions, in addition to four hydrogen bonds formed by each gp47 subunit. Similarly, the T4 Soc proteins interact with the major capsid proteins to stabilize the inter-capsomer interactions, which enable the T4 phage to survive under extreme conditions (Chen et al., 2017; Qin et al., 2010). It is possible that Mic1 cement protein gp47 has the same function of reinforcing the capsid assembly, even though it sticks on the capsid via a different pattern. Notably, the phages T4, phi812, and epsilon15 that harbor a cement protein have a relatively stable icosahedral capsid (Baker et al., 2013; Chen et al., 2017; Novacek et al., 2016). Therefore, we speculate that the cement protein gp47 possesses a similar function that stabilizes the icosahedral-shaped capsid of Mic1.

Assembly of Mic1 Capsid

Based on the structural information, we proposed a putative assembly process of Mic1 capsid (Figure 7). First, the highly flexible P domains and E loops of gp40 subunits surround six-fold symmetric A domains at the center to form the hexons (Figures 7A and 7B). Thanks to the plasticity of the A domain, more curvature could be introduced at the five-fold vertices to form the pentons (Figures 7A and 7B). Thereafter, each of three hexons are interlocked via extensive interactions in a cyclic tail-in-mouth pattern around the three-fold axis, in addition to the swapped antiparallel N arms at the interface between each pair of neighboring hexons (Figure 7C). Eventually, the hexons assemble to form an icosahedral lattice, which recruits 11 pentons and one

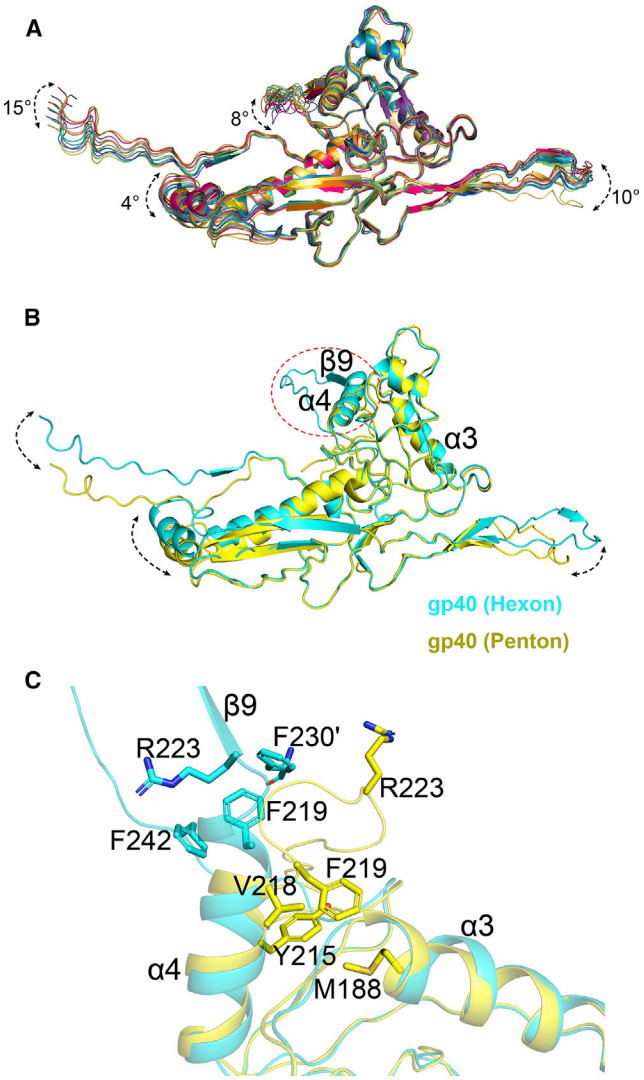

Figure 4. Conformational Flexibilities of the Major Capsid Protein gp40

(A) Superposition of 12 gp40 molecules of the two hexons within an asymmetric unit. The 12 gp40 subunits are colored differently.

(B) Superposition of one gp40 subunit in the hexon and penton, colored cyan and yellow, respectively.

(C) Structural variations of the A domain of gp40 in the hexon and penton, colored in cyan and yellow, respectively. Residues with conformational changes are shown as sticks. The residue Phe230 from the adjacent subunit of a hexon is labeled with a prime.

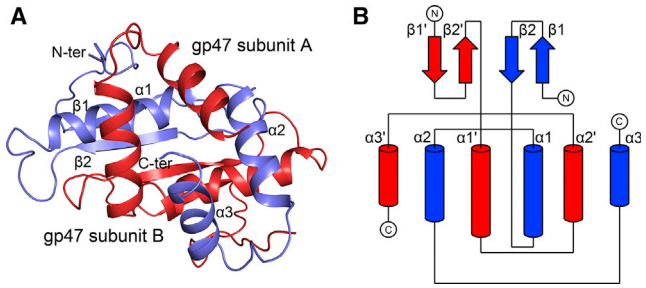

Figure 5. Structure of the Cement Protein gp47

(A) Overall structure of the dimeric cement protein gp47. The subunits A and B of gp47 are colored red and blue, respectively.

(B) Topology diagram of the dimeric gp47.

See also Figure S6 and Table S3.

portal at the vertices to form a closed isometric capsid (Figure 7C). In addition, each pair of capsomers is glued by the dimeric cement protein gp47 at the two-fold axis (Figure 7D). This mortise-and-tenon structure gives Mic1 a relatively stable and rigid capsid. In fact, Mic1 possesses a relatively high melting temperature up to ~79°C, as calculated by the fluorescence-based thermostability assays (Figure S7). Previous studies suggested that the capsid assembly process also requires scaffold proteins (Dokland, 1999), which function as chaperones to recruit pentons and hexons at the 12-fold symmetric connector that initiates the assembly process. Sequence analysis indicated that Mic1 also encodes a hypothetical chaperone gp42 (GenBank: MN013189). Notably, the capsid shell may undergo further conformational changes to enable the package of DNA (Fokine and Rossmann, 2014) and the maturation of the phage.

DISCUSSION

Here we identified a new freshwater cyanophage, Mic1, in the Siphoviridae family that infects *Microcystis*. The capsid structure demonstrated an icosahedral assembly with a triangulation number T of 13. The major capsid protein gp40 of Mic1 adopts an HK97-like fold (Figure S8), a highly conserved fold of all bacteriophages that was first identified the phage HK97 (Zhou and Chiou, 2015). In addition, the major capsid proteins of herpesvirus also have an HK97-like fold (Baker et al., 2005). A structure-based phylogenetic tree suggested that all these capsid proteins might evolve from a common ancestor (Baker et al., 2005; Bamford et al., 2005). Despite sharing a canonical HK97-like fold, gp40 harbors a unique insertion segment and has no interaction with the neighboring subunits. It is different from the insertion domains of other phages that contribute to the intra- or inter-capsomer interactions (Hryc et al., 2017; Zhao et al., 2017). Moreover, the cement protein gp47 in our structure adopts a novel fold distinct from all proteins of known structure. The gene encoding this novel cement protein might be acquired very early from the host cyanobacteria, most likely due to co-evolution and gene transfer (Lindell et al., 2007). In fact, the marine cyanophage Syn5 also harbors two unique cement proteins, gp55 and gp58, which bind to the major capsid proteins in diagonal positions within a hexon, presumably to stabilize the intra-capsomer subunits (Gipson et al., 2015).

The structure of Mic1 revealed a unique assembly pattern of capsid subunits that has not been observed in other phages of known structure. The capsid is assembled via non-covalent interactions, but displays a relatively stable structure to maintain the high internal pressure for DNA packaging. First, the E loops and P domains of gp40 forge extensive interactions to form the mortise-and-tenon joints at three-fold regions, which were proposed to be the weakest sites for the icosahedral capsids (Mateu, 2013; Zandi and Reguera, 2005). The HK97 phage adopts the isopeptide bonds to stabilize the three-fold sites (Wikoff

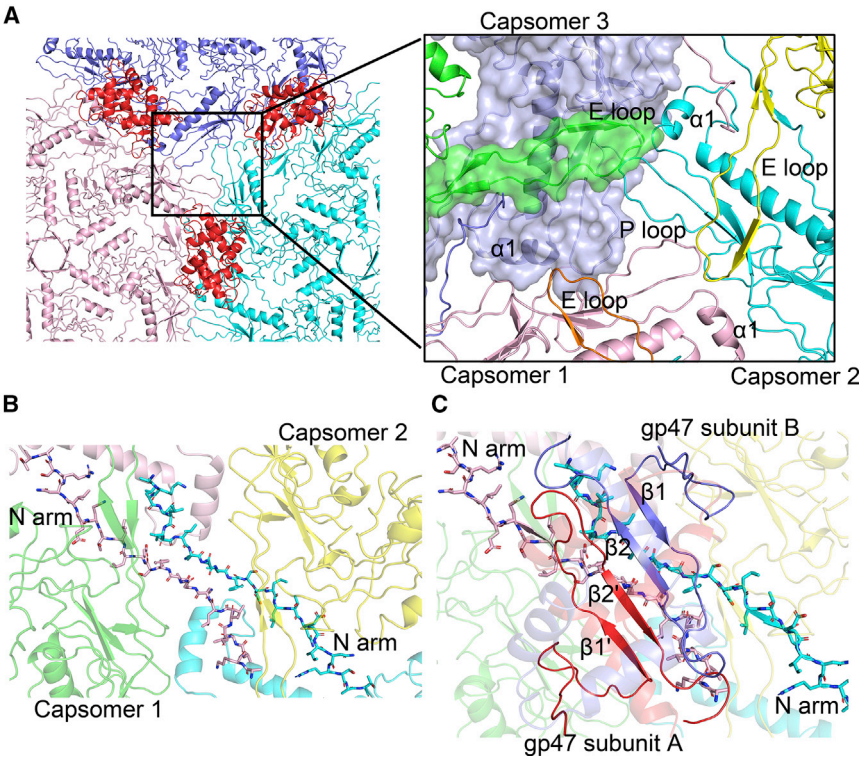

Figure 6. Assembly of Mic1 Capsid

(A) The inter-capsomer interface viewed along the three-fold axis. The three capsomers are colored differently (capsomer 1 in pink, capsomer 2 in cyan, and capsomer 3 in blue). The inset shows a zoom-in view of the inter-capsomer interface, with one capsomer shown in semi-transparent surface and the other two shown in cartoon. To distinguish the interactions, each of the E loops of the three capsomers are colored orange, yellow, and green, respectively.

(B) The swapped antiparallel N arms extending to the neighboring capsomer are shown as sticks.

(C) A gp47 dimer sticks to the swapped N arms.

See also Figure S7.

et al., 2000), whereas many other phages utilize the non-covalently bound trimeric cement proteins, such as Soc in T4 phage (Chen et al., 2017). Second, the extended N arms at the two-fold axis interact with multiple subunits via inter- and intra-capsomer interactions, thus providing a long-distance reinforcing mechanism, similar to the function of N arms in sf6 phage (Zhao et al., 2017). In addition, the two-fold symmetric N arms of Mic1 also function as a pedestal to recruit the dimeric cement protein gp47. Distinct from the previously reported dimeric cement proteins, such as gp10 of epsilon15 (Baker et al., 2013) and Bbp16 of BPP-1 phage (Zhang et al., 2013), the gp47 displays a highly entangled dimer, which functions as a strong glue to stabilize the two adjacent capsomers. The structural variations in the major capsid proteins combined with cement/decorating proteins, enable the phage to form a stable yet plastic capsid, which is necessary to efficiently accommodate the genome package and survive in various environments (Mateu, 2013; Suhanovsky and Teschke, 2015).

In summary, we demonstrated the cryo-EM structure of a freshwater cyanophage that specifically infects *Microcystis*, a dominant species of algal blooms in the lakes of southern China. Our findings provided a platform to study the recognition and co-evolution between bloom-forming cyanobacteria and corresponding cyanophages. However, further investigations of their physiological functions and identification of more cyanophages are necessary for better understanding of host-cyanophage interactions and their future applications to the control of algal blooms.

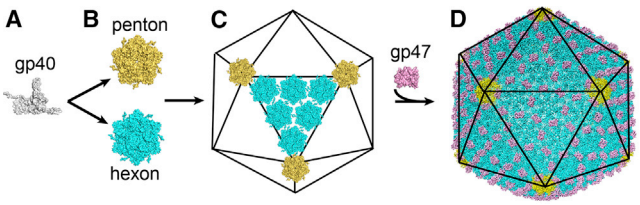

Figure 7. A Schematic Model of the Assembly of Mic1 Capsid

(A) The major capsid protein gp40 (gray) harbors an HK97-like fold.

(B) The gp40 subunits are organized into pentons (yellow) and hexons (cyan) to initiate the capsid assembly.

(C) The neighboring capsomers are interlocked by the double-layered interfaces and the extended N arms in a mortise-and-tenon pattern to form the assembly core of the capsid.

(D) Recruitment of the dimeric cement protein gp47 at the two-fold site further reinforces the capsid stability and thus accomplishes the capsid assembly. The gp40 and gp47 proteins are shown in surface mode.

STAR★METHODS

Detailed methods are provided in the online version of this paper and include the following:

- KEY RESOURCES TABLE
- LEAD CONTACT AND MATERIALS AVAILABILITY
- EXPERIMENTAL MODEL AND SUBJECT DETAILS
  - Cyanobacterial Strains and Growth Conditions
- METHOD DETAILS
  - Screening of Cyanophages
  - Growth Curve Measurement
  - Ultrathin Sections
  - Cyanophage Purification
  - Protein Gel Electrophoresis and Mass Spectrometry
  - Fluorescence-Based Thermal Shift Assay
  - Negative-Stain EM
  - Cryo-EM Sample Preparation, Data Collection and Processing
  - Model Building and Refinement
- QUANTIFICATION AND STATISTICAL ANALYSIS
- DATA AND CODE AVAILABILITY

SUPPLEMENTAL INFORMATION

Supplemental Information can be found online at https://doi.org/10.1016/j.str.2019.07.003.

ACKNOWLEDGMENTS

We thank Dr. Xueming Li and Mingxu Hu at Tsinghua University for the advice on using THUNDER to refine the models, Boling Zhu and Xiaojun Huang for technical support on cryo-EM data collection at the Center for Biological Imaging, Core Facilities for Protein Science at the Institute of Biophysics (IBP), Chinese Academy of Sciences, and Peiping Tang for cryo-EM sample examination at the Center for Integrative Imaging, Hefei National Laboratory for Physical Sciences at the Microscale, University of Science and Technology of China. We also thank Dr. Chen Ding at Fudan University for the mass spectrometric analysis. This work was supported by the Ministry of Science and Technology of China (http://www.most.gov.cn, grant nos. 2018YFA0903100 and 2016YFA0400900), the National Natural Science Foundation of China (http://www.nsfc.gov.cn, grant nos. 31630001 and 31621002), and the Chinese Academy of Sciences (the Innovation Academy for Seed Design).

AUTHOR CONTRIBUTIONS

C.-Z.Z. and Y.C. conceived, designed, and supervised the project. C.-Z.Z., Y.C., Y.-L.J., and H.J. analyzed data and wrote the manuscript. H.J., F.Y., J.-T.Z., W.-F.L., K.Z., and J.J. performed the cyanophage isolation and characterization experiments. H.J. purified and analyzed the samples. Y.-L.J. conducted the data acquisition, structure determination, and model building. All authors discussed the data and read the manuscript.

DECLARATION OF INTERESTS

The authors declare no competing interests.

Received: March 20, 2019
Revised: June 11, 2019
Accepted: July 12, 2019
Published: August 1, 2019

REFERENCES

Ackermann, H.W. (2007). 5500 Phages examined in the electron microscope. Arch. Virol. *152*, 227–243.

Adams, P.D., Afonine, P.V., Bunkoczi, G., Chen, V.B., Davis, I.W., Echols, N., Headd, J.J., Hung, L.W., Kapral, G.J., Grosse-Kunstleve, R.W., et al. (2010). PHENIX: a comprehensive Python-based system for macromolecular structure solution. Acta Crystallogr. D Biol. Crystallogr. *66*, 213–221.

Baker, M.L., Hryc, C.F., Zhang, Q.F., Wu, W.M., Jakana, J., Haase-Pettingell, C., Afonine, P.V., Adams, P.D., King, J.A., Jiang, W., et al. (2013). Validated near-atomic resolution structure of bacteriophage epsilon15 derived from cryo-EM and modeling. Proc. Natl. Acad. Sci. U S A *110*, 12301–12306.

Baker, M.L., Jiang, W., Rixon, F.J., and Chiu, W. (2005). Common ancestry of herpesviruses and tailed DNA bacteriophages. J. Virol. *79*, 14967–14970.

Bamford, D.H., Grimes, J.M., and Stuart, D.I. (2005). What does structure tell us about virus evolution? Curr. Opin. Struct. Biol. *15*, 655–663.

Chen, V.B., Arendall, W.B., Headd, J.J., Keedy, D.A., Immormino, R.M., Kapral, G.J., Murray, L.W., Richardson, J.S., and Richardson, D.C. (2010). MolProbity: all-atom structure validation for macromolecular crystallography. Acta Crystallogr. D Biol. Crystallogr. *66*, 12–21.

Chen, Y.W., Qin, B.Q., Teubner, K., and Dokulil, M.T. (2003). Long-term dynamics of phytoplankton assemblages: *Microcystis*-domination in Lake Taihu, a large shallow lake in China. J. Plankton Res. *25*, 445–453.

Chen, Z.G., Sun, L., Zhang, Z.H., Fokine, A., Padilla-Sanchez, V., Hanein, D., Jiang, W., Rossmann, M.G., and Rao, V.B. (2017). Cryo-EM structure of the bacteriophage T4 isometric head at 3.3-angstrom resolution and its relevance to the assembly of icosahedral viruses. Proc. Natl. Acad. Sci. U S A *114*, 8184–8193.

Dearborn, A.D., Wall, E.A., Kizziah, J.L., Klenow, L., Parker, L.K., Manning, K.A., Spilman, M.S., Spear, J.M., Christie, G.E., and Dokland, T. (2017). Competing scaffolding proteins determine capsid size during mobilization of *Staphylococcus aureus* pathogenicity islands. Elife *6*, e30822.

Dokland, T. (1999). Scaffolding proteins and their role in viral assembly. Cell. Mol. Life Sci. *56*, 580–603.

Emsley, P., and Cowtan, K. (2004). Coot: model-building tools for molecular graphics. Acta Crystallogr. D Biol. Crystallogr. *60*, 2126–2132.

Fokine, A., Islam, M.Z., Zhang, Z.H., Bowman, V.D., Rao, V.B., and Rossmann, M.G. (2011). Structure of the three N-terminal immunoglobulin domains of the highly immunogenic outer capsid protein from a T4-Like Bacteriophage. J. Virol. *85*, 8141–8148.

Fokine, A., and Rossmann, M.G. (2014). Molecular architecture of tailed double-stranded DNA phages. Bacteriophage *4*, e28281.

Gipson, P., Baker, M.L., Raytcheva, D., Haase-Pettingell, C., Piret, J., King, J.A., and Chiu, W. (2015). Protruding knob-like proteins violate local symmetries in an icosahedral marine virus. Nat. Commun. *6*, 4278.

Guo, F., Liu, Z., Fang, P.A., Zhang, Q.F., Wright, E.T., Wu, W.M., Zhang, C., Vago, F., Ren, Y., Jakana, J., et al. (2014). Capsid expansion mechanism of bacteriophage T7 revealed by multistate atomic models derived from cryo-EM reconstructions. Proc. Natl. Acad. Sci. U S A *111*, 4606–4614.

Holm, L., and Sander, C. (1993). Protein-structure comparison by alignment of distance matrices. J. Mol. Biol. *233*, 123–138.

Hryc, C.F., Chen, D.H., Afonine, P.V., Jakana, J., Wang, Z., Haase-Pettingell, C., Jiang, W., Adams, P.D., King, J.A., Schmid, M.F., et al. (2017). Accurate model annotation of a near-atomic resolution cryo-EM map. Proc. Natl. Acad. Sci. U S A *114*, 3103–3108.

Hu, M.X., Yu, H.K., Gu, K., Wang, Z., Ruan, H.B., Wang, K.P., Ren, S.Y., Li, B., Gan, L., Xu, S.Z., et al. (2018). A particle-filter framework for robust cryo-EM 3D reconstruction. Nat. Methods *15*, 1083–1089.

Huisman, J., Codd, G.A., Paerl, H.W., Ibelings, B.W., Verspagen, J.M.H., and Visser, P.M. (2018). Cyanobacterial blooms. Nat. Rev. Microbiol. *16*, 471–483.

Lecompte, O., Ripp, R., Thierry, J.C., Moras, D., and Poch, O. (2002). Comparative analysis of ribosomal proteins in complete genomes: an example of reductive evolution at the domain scale. Nucleic Acids Res. *30*, 5382–5390.

Lindell, D., Jaffe, J.D., Coleman, M.L., Futschik, M.E., Axmann, I.M., Rector, T., Kettler, G., Sullivan, M.B., Steen, R., Hess, W.R., et al. (2007). Genome-wide expression dynamics of a marine virus and host reveal features of co-evolution. Nature *449*, 83–86.

Liu, W., and Qiu, R. (2007). Water eutrophication in China and the combating strategies. J. Chem. Technol. Biotechnol. *82*, 781–786.

Liu, X.A., Zhang, Q.F., Murata, K., Baker, M.L., Sullivan, M.B., Fu, C., Dougherty, M.T., Schmid, M.F., Osburne, M.S., Chisholm, S.W., et al. (2010). Structural changes in a marine podovirus associated with release of its genome into *Prochlorococcus*. Nat. Struct. Mol. Biol. *17*, 830–876.

Mateu, M.G. (2013). Assembly, stability and dynamics of virus capsids. Arch. Biochem. Biophys. *531*, 65–79.

Muhling, M., Fuller, N.J., Millard, A., Somerfield, P.J., Marie, D., Wilson, W.H., Scanlan, D.J., Post, A.F., Joint, I., and Mann, N.H. (2005). Genetic diversity of marine *Synechococcus* and co-occurring cyanophage communities: evidence for viral control of phytoplankton. Environ. Microbiol. *7*, 499–508.

Nagasaki, K., and Yamaguchi, M. (1997). Isolation of a virus infectious to the harmful bloom causing microalga *Heterosigma akashiwo* (Raphidophyceae). Aquat. Microb. Ecol. *13*, 135–140.

Novacek, J., Siborova, M., Benesik, M., Pantucek, R., Doskar, J., and Plevka, P. (2016). Structure and genome release of Twort-like *Myoviridae* phage with a double-layered baseplate. Proc. Natl. Acad. Sci. U S A *113*, 9351–9356.

Paerl, H.W. (2017). Controlling cyanobacterial harmful blooms in freshwater ecosystems. Microb. Biotechnol. *10*, 1106–1110.

Pettersen, E.F., Goddard, T.D., Huang, C.C., Couch, G.S., Greenblatt, D.M., Meng, E.C., and Ferrin, T.E. (2004). UCSF chimera—a visualization system for exploratory research and analysis. J. Comput. Chem. *25*, 1605–1612.

Qin, L., Fokine, A., O'Donnell, E., Rao, V.B., and Rossmann, M.G. (2010). Structure of the small outer capsid protein, soc: a clamp for stabilizing capsids of T4-like phages. J. Mol. Biol. *395*, 728–741.

Rasmussen, B., Fletcher, I.R., Brocks, J.J., and Kilburn, M.R. (2008). Reassessing the first appearance of eukaryotes and cyanobacteria. Nature *455*, 1101–1109.

Rohou, A., and Grigorieff, N. (2015). CTFFIND4: Fast and accurate defocus estimation from electron micrographs. J. Struct. Biol. *192*, 216–221.

Safferman, R.S., and Morris, M.E. (1963). Algal virus - isolation. Science *140*, 679–680.

Scheres, S.H.W. (2012). RELION: Implementation of a Bayesian approach to cryo-EM structure determination. J. Struct. Biol. *180*, 519–530.

Shane, M.S. (1971). Distribution of blue-green algal viruses in various types of natural waters. Water Res. *5*, 711–716.

Shevchenko, A., Tomas, H., Havlis, J., Olsen, J.V., and Mann, M. (2006). In-gel digestion for mass spectrometric characterization of proteins and proteomes. Nat. Protoc. *1*, 2856–2860.

Suhanovsky, M.M., and Teschke, C.M. (2015). Nature's favorite building block: Deciphering folding and capsid assembly of proteins with the HK97-fold. Virology *479*, 487–497.

Sullivan, M.B., Waterbury, J.B., and Chisholm, S.W. (2003). Cyanophages infecting the oceanic cyanobacterium *Prochlorococcus*. Nature *424*, 1047–1051.

Suttle, C.A. (2005). Viruses in the sea. Nature *437*, 356–361.

Suttle, C.A., and Chan, A.M. (1993). Marine cyanophages infecting oceanic and coastal strains of *Synechococcus*-abundance, morphology, cross-infectivity and growth-characteristics. Mar. Ecol. Prog. Ser. *92*, 99–109.

Suttle, C.A., and Chan, A.M. (1994). Dynamics and distribution of cyanophages and their effect on marine *Synechococcus* Spp. Appl. Environ. Microbiol. *60*, 3167–3174.

Thompson, L.R., Zeng, Q., Kelly, L., Huang, K.H., Singer, A.U., Stubbe, J., and Chisholm, S.W. (2011). Phage auxiliary metabolic genes and the redirection of cyanobacterial host carbon metabolism. Proc. Natl. Acad. Sci. U S A *108*, 757–764.

Wang, Z.Q., Hardies, S.C., Fokine, A., Klose, T., Jiang, W., Cho, B.C., and Rossmann, M.G. (2018). Structure of the marine *Siphovirus* TW1: evolution of capsid-stabilizing proteins and tail spikes. Structure *26*, 238–248.

Weinbauer, M.G. (2004). Ecology of prokaryotic viruses. FEMS Microbiol. Rev. *28*, 127–181.

Wikoff, W.R., Liljas, L., Duda, R.L., Tsuruta, H., Hendrix, R.W., and Johnson, J.E. (2000). Topologically linked protein rings in the bacteriophage HK97 capsid. Science *289*, 2129–2133.

Xiao, X., Zeng, Q., Zhang, R., and Jiao, N. (2018). *Prochlorococcus* viruses—from biodiversity to biogeochemical cycles. Sci. China Earth Sci. *61*, 1728–1736.

Zandi, R., and Reguera, D. (2005). Mechanical properties of viral capsids. Phys. Rev. E *72*, 021971.

Zeng, Q.L., and Chisholm, S.W. (2012). Marine viruses exploit their host's two-component regulatory system in response to resource limitation. Curr. Biol. *22*, 124–128.

Zhang, Q.Y., and Gui, J.F. (2018). Diversity, evolutionary contribution and ecological roles of aquatic viruses. Sci. China Life Sci. *61*, 1486–1502.

Zhang, X., Guo, H.T., Jin, L., Czornyj, E., Hodes, A., Hui, W.H., Nieh, A.W., Miller, J.F., and Zhou, Z.H. (2013). A new topology of the HK97-like fold revealed in *Bordetella* bacteriophage by cryoEM at 3.5 angstrom resolution. Elife *2*, e01299.

Zhao, H.Y., Li, K.P., Lynn, A.Y., Aron, K.E., Yu, G.M., Jiang, W., and Tang, L. (2017). Structure of a headful DNA-packaging bacterial virus at 2.9 angstrom resolution by electron cryo-microscopy. Proc. Natl. Acad. Sci. U S A *114*, 3601–3606.

Zhou, Z.H., and Chiou, J. (2015). Protein chainmail variants in dsDNA viruses. AIMS Biophys. *2*, 200–218.

Zhou, Z.H., Hui, W.H., Shah, S., Jih, J., O'Connor, C.M., Sherman, M.B., Kedes, D.H., and Schein, S. (2014). Four levels of hierarchical organization, including noncovalent chainmail, brace the mature tumor herpesvirus capsid against pressurization. Structure *22*, 1385–1398.

STAR★METHODS

KEY RESOURCES TABLE

REAGENT or RESOURCE	SOURCE	IDENTIFIER
Bacterial and Virus Strains		
Microcystis wesenbergii strain FACHB1318	Institute of Hydrobiology, Chinese Academy of Sciences	N/A
Microcystis wesenbergii strain FACHB1339	Institute of Hydrobiology, Chinese Academy of Sciences	N/A
Mic1	This paper	N/A
Chemicals, Peptides, and Recombinant Proteins		
OsO4	Sigma-Aldrich	Cat#20816-12-0
Spurr resin (mixture)	SPI-CHEM	Cat#41638-13-5
		Cat#28928-97-4
		Cat#108-01-0
		Cat#2386-87-0
CsCl	Sigma-Aldrich	Cat#7641-17-8
SYPRO Orange	Thermo Fisher	S6650
Deposited Data		
Coordinates of Mic1 capsid	This paper	PDB: 6J3Q
Cryo-EM map of Mic1 capsid	This paper	EMD-9774
Software and Algorithms		
OriginPro	N/A	https://www.originlab.com/Origin; RRID: SCR_014212
CTFFIND4	Rohou and Grigorieff, 2015	http://grigoriefflab.janelia.org/ctffind4; RRID: SCR_016732
RELION	Scheres, 2012	http://www2.mrc-lmb.cam.ac.uk/relion; RRID: SCR_016274
COOT	Emsley and Cowtan, 2004	https://www2.mrc-lmb.cam.ac.uk/personal/pemsley/coot/; RRID: SCR_014222
PHENIX	Adams et al., 2010	https://www.phenix-online.org; RRID: SCR_014224
UCSF Chimera	Pettersen et al., 2004	https://www.cgl.ucsf.edu/chimera; RRID: SCR_004097
PyMOL	Schrödinger	http://www.pymol.org; RRID: SCR_000305
Other		
R3.5/1 200 mesh copper grids	Quantifoil	Q250CR-35

LEAD CONTACT AND MATERIALS AVAILABILITY

Further information and requests for resources and reagents should be directed to and will be fulfilled by the Lead Contact, Cong-Zhao Zhou (zcz@ustc.edu.cn).

EXPERIMENTAL MODEL AND SUBJECT DETAILS

Cyanobacterial Strains and Growth Conditions

The cyanobacterial strains used in this study were listed in Table S1. Strains were obtained from the Freshwater Algae Culture Collection at the Institute of Hydrobiology, Chinese Academy of Sciences. All strains were cultured in BG-11 medium at 28°C under a 14-hr light/10-hr dark cycle using 30-40 μmol photons/m2/s with cool white fluorescent illumination.

METHOD DETAILS

Screening of Cyanophages

Water samples were collected at ten spots in the Lake Chaohu (31°25'N–31°43'N, 117°16'E–117°51'E). The water samples were sequentially filtered by the cellulose nitrate membranes at the cutoff of 1.2, 0.45 and 0.22 μm, respectively, to remove the large impurities. Then 0.2 mL of the filtered water samples was individually added to 0.8 mL of different cyanobacterial strains at exponential growth phase in 24-well microplates. Optical microscopy was used to check the growth status of cyanobacteria every day in two weeks. Once the cells were lysed by the water samples, the lysate was subject to four rounds of cyanophage purification by extinction dilution procedure, as described previously (Nagasaki and Yamaguchi, 1997; Suttle and Chan, 1993). In details, a serial 10-fold dilutions of the lysate at 0.1 mL was added to the 0.9 mL medium cultured by the fresh cyanobacterial strains at exponential growth phase. After grown in the 24-well microplate for about one week, the cells were lysed again with the maximal dilution rate of $1/10^8$. Then the cell lysate under the maximal dilution rate was applied to the next round of phage amplification. After four rounds of purification, the single colony of Mic1 was obtained in agar plate, which was further confirmed by negative-stain electron microscopy.

Growth Curve Measurement

One-step growth curve was constructed to evaluate the latent period and burst size of Mic1. The *M. wesenbergii* cells (5.6×10^6 cells/mL) were inoculated with Mic1 (6×10^6 pfu/mL) at a multiplicity of infection (MOI) of ~1.07. The medium cultured with uninfected *M. wesenbergii* was used as the control. To measure the growth curve, 0.1 mL sample was taken from the medium every four hours in a total period of 28 hr. The density of *M. wesenbergii* cells was calculated by a hemocytometer (Shanghai Medical Optical Instrument Factory), whereas the viral titer was measured by plaque assays on the solid medium. The growth curve was drawn by the OriginPro 8.5 program, and three independent experiments were performed to calculate the means and standard deviations.

Ultrathin Sections

The infection of Mic1 to *M. wesenbergii* was confirmed by ultrathin section. The *M. wesenbergii* cells were infected by Mic1 at MOI of 2. After 20 hr cultivation, the cells were harvested by centrifugation at 3000 g for 10 min. The collected cells were fixed in 2% (wt/vol) paraformaldehyde and 2.5% (wt/vol) glutaraldehyde in PBS buffer at pH 7.4 for 2 hr at 25°C and then overnight at 4°C. Then the samples were washed with PBS buffer three times to remove the paraformaldehyde and glutaraldehyde buffer, and fixed with 2% OsO_4 in PBS buffer overnight at 25°C. After washes for three times with PBS buffer, the samples were dehydrated in a graded ethanol series (30 to 100%) and transferred to acetone for 20 min. After transferred to 1:1 mixture of acetone and Spurr resin for 2 hr, the specimen was embedded in Spurr resin overnight at 25°C. The cubes were heated at 70°C for more than 9 hr, then sectioned in LEICA EM UC7 ultratome. Ultrathin sections were stained with 2% uranium acetate and 3% lead citrate and observed at FEI Technai G2 120 KV transmission electron microscope.

Cyanophage Purification

One liter of cell lysate after Mic1 infection was centrifuged at 8,000 g for 10 min at 4°C to remove cellular debris. Afterwards, DNase I and RNase A at a final concentration of 1 μg/ml were added in the supernatant and incubated at 25°C for 2 hr. The Mic1 particles were enriched by centrifugation at 7,000 g for 16 hr at 4°C. The pellet containing Mic1 was resuspended in SM buffer (50 mM Tris-HCl pH7.5, 100 mM NaCl, 10 mM $MgSO_4$). The samples were subject to another round of centrifugation at 10,000 g, 4°C for 20 min to remove the remaining cell debris. The supernatant containing Mic1 was concentrated and loaded onto a discrete density gradient of CsCl (1.3, 1. 5, 1.6 and 1.65 g/ml). The gradient was further centrifuged at 100,000 g for 2 hr at 4°C. A visible band corresponding to Mic1 was collected using Density Gradient Fractionation System (BR-188, BRANDEL). The purified Mic1 samples were dialyzed in SM buffer at 4°C overnight to remove CsCl.

Protein Gel Electrophoresis and Mass Spectrometry

The purified Mic1 particles were mixed with an equal volume of 2× electrophoresis loading buffer (62.5 mM Tris-HCl, 2% polyacrylamide, 10% glycerol, 2% 2-mercaptoethanol and 0.1% bromophenol blue, pH 6.8) at 95°C for 10 min, and loaded onto a 4-12% gradient polyacrylamide gel (Genscript). Protein bands were visualized by Coomassie Blue staining. Protein molecular mass standards ranging from 14.4 to 116 kDa (Invitrogen) were used. Then the gel was manually excised, digested with trypsin, and analyzed by liquid chromatography/mass spectrometry (LC-MS/MS) using ion-trap mass spectrometer (Thermo LUMOS) in Fudan University (Shevchenko et al., 2006). The detected peptide fragments were mapped to the 98 hypothetical proteins encoded by the Mic1 genome.

Fluorescence-Based Thermal Shift Assay

Thermal shift assays were performed with purified cyanophage Mic1 at a concentration of about 10^{12} particles per mL in SM buffer and SYPRO Orange (Invitrogen). Solution mixtures were prepared and pipetted into 386-well PCR plates at a final volume of 10 μL for each well. The plate was heated from 25 to 99°C with a heating rate of 1.85°C/min on a real-time PCR machine (LightCycler, Roche). The fluorescence intensity was measured with Ex/Em: 490/530 nm. The melting curve was calculated by the program OriginPro 8.5.

Negative-Stain EM

For examination of cyanophage Mic1, the purified sample was visualized using negative-stain transmission electron microscopy. The Mic1 sample was incubated in a 400-mesh carbon-coated glow-discharged copper grid for 30 sec and stained with 2% (wt/vol) uranium acetate solution for 1 min. The negatively stained images were captured with a FEI Technai G2 120 KV transmission electron microscope.

Cryo-EM Sample Preparation, Data Collection and Processing

Purified Mic1 sample was concentrated to about 10^{12} particles per mL, and was frozen in liquid ethane by using Vitrobot (FEI). A sample of 3.5 μL was loaded onto a fresh glow-discharged 200-mesh holey copper grid (Quantifoil R3.5/1) coated by a layer of continuous carbon. Grids were blotted for 4 sec with a blot force of 1 in 100% relative humidity at 8°C. The grids were stored in liquid nitrogen for future use.

Cryo-EM data sets were collected at 300 kV with a Titan Krios microscope (FEI) at the Institute of Biophysics (IBP), Chinese Academy of Sciences (CAS). Movies (32 frames, each 0.18 sec, total dose 25 e/Å^2) were recorded using an electron-counting K2 detector at the super-resolution counting mode with a defocus range of 1 to 2 μm. Automated single-particle data acquisition was performed with SerialEM, with a nominal magnification of 59,000×, which yields a final pixel size of 1.36 Å. A total of 1935 micrographs were recorded and the defocus value for each micrograph was determined using CtfFind (Rohou and Grigorieff, 2015). Approximately 18,800 particles were boxed using RELION (Scheres, 2012) and then were checked one by one to remove the overlapped particles. After several rounds of 2D and 3D classifications by RELION, eventually 9702 good particles were selected to perform the 3D refinement. The RELION software gave to a reconstruction of ~4.2 Å resolution with icosahedral symmetry imposed. Next, we performed the defocus refinement implemented in THUNDER (Hu et al., 2018), and finally yielding a resolution up to 3.5 Å, as determined by Golden standard Fourier shell correlation using the 0.143 threshold. We used the program of post-process in RELION to evaluate the resolution, and performed the map sharpening at the B-factor of -125.62.

Model Building and Refinement

The map showed clear continuous density which enabled us to assign the main-chain and bulky side-chain residues. Bioinformatics analysis indicated that gp40 is the major capsid protein, We first manually built an all-alanine model into the map using COOT (Emsley and Cowtan, 2004). The side-chains were then assigned by using Sequence_From_Map in Phenix, and further manually adjusted with the assistance of bulky residues. Afterwards, the other 12 gp40 subunits within an asymmetric unit were built by individually fitting the gp40 model into the map, followed by the manual refinement in COOT. The map of an asymmetric unit was then cut out, and was subject to the automatic refinement by Real-space refinement in Phenix. After manual building of 13 gp40 subunits in an asymmetric unit, there still obviously exist several extra continuous densities, in which an all-alanine model was *ab initio* built into using COOT. Then we applied the Sequence_From_Map program implemented in PHENIX (Adams et al., 2010) to determine which protein best fits the density, with the all-alanine model combined with the genome sequence of Mic1. At last, gp47 was found to fit the density well and residue assignment was performed manually using COOT. The refined models of gp40 and gp47 were further fitted into other parts of an asymmetric unit using CHIMERA (Pettersen et al., 2004). Models of an asymmetric unit were further improved by iterative positional and B-factor refinement in real space using PHENIX, rebuilding in COOT, and evaluated by Molprobity (Chen et al., 2010). Refinement statistics were listed in Table 1. The structure figures were prepared by using the programs CHIMERA and PyMOL (www.pymol.org).

QUANTIFICATION AND STATISTICAL ANALYSIS

Data of growth curve assays were expressed as means ± the standard deviation from three independent experiments. Data of melting curve were calculated by the Boltzmann equation from three independent experiments. Statistical analysis was performed in OriginPro. No data were excluded for analysis.

DATA AND CODE AVAILABILITY

The structure of Mic1 capsid has been deposited in the Protein Data Bank (PDB; accession code 6J3Q). The cryo-EM density map has been deposited in the Electron Microscopy Data Bank (accession code EMD-9774).